JOURNAL OF PROPULSION AND POWER
Vol. 24, No. 3, May–June 2008

Internal Flow Dynamics in a Valveless Airbreathing Pulse Detonation Engine

Fuhua Ma,* Jeong-Yeol Choi,† and Vigor Yang‡
Pennsylvania State University, University Park, Pennsylvania 16802

DOI: 10.2514/1.29957

The internal flow dynamics in a valveless airbreathing pulse detonation engine operating on ethylene fuel is studied numerically. The system involves no mechanical valves in the air flowpath, and the isolation between the inlet and combustor is achieved through gas-dynamic means. The valve operation timing for the fuel injection and initiator is determined based on the local flow conditions. The analysis accommodates the full conservation equations in axisymmetric coordinates and takes into account simplified finite-rate chemistry and variable properties for an ethylene/air/oxygen system. The detailed flow evolution and detonation dynamics during the limit-cycle operation is explored systematically. The calculated pressure history and propulsive performance agree well with experimental data. A sensitivity study of operation timing is also conducted to further elucidate the system dynamics and to provide guidelines for engine design optimization.

Nomenclature

A = preexponential factor or area
e_t = specific total energy
F^g = instantaneous gross thrust
$\bar{F}^g$ = cycle-averaged gross thrust
g = gravitational acceleration
I^g_{sp} = gross specific impulse
m = mass
$\dot{m}_C$ = mass flow rate for main combustor fuel injection
$\dot{m}_I$ = mass flow rate for initiator injection
p = pressure
p_b = backpressure or ambient pressure
p_{00} = total pressure at entrance of inlet
q = heat release per unit mass of reactant
R = gas constant
T = temperature
T_a = activation temperature
T_{0C} = total temperature for main combustor injection
T_{0I} = total temperature for initiator injection
T_{00} = total temperature at entrance of inlet
t = time
u = axial velocity
V = volume
v = radial velocity
W = molecular weight
x = axial coordinate
y = radial coordinate
Z_i = mass fraction of nominal species i
γ = specific heat ratio
ρ = density
τ_{cycle} = cycle period
τ_{delay} = period between the start of combustor and initiator filling
τ_{fill} = combustor filling period
τ_{open0} = period during which initiator is charging with air
τ_{open1} = period during which initiator is charging with C_2H_4/air mixture
τ_{open2} = period during which initiator is charging with oxygen-enriched C_2H_4/air mixture
τ_{purge} = period during which main injector is closed
$\dot{\omega}$ = species mass production rate

Subscripts

C = combustor
I = initiator
i = index of nominal species; 1 for stoichiometric C_2H_4/air mixture, 2 for products of C_2H_4/air mixture, 3 for stoichiometric C_2H_4/O_2 mixture, 4 for products of C_2H_4/O_2 mixture, and 5 for air

I. Introduction

PULSE detonation engines (PDEs) are unsteady propulsion devices that produce thrust by using repetitive detonation. Over the past decade, PDEs have attracted considerable attention because of their potential advantages in thermodynamic cycle efficiency, hardware simplicity, operational stability, and reliability [1,2]. To prevent inlet unstart caused by high-pressure detonation products, PDEs generally require an inlet/combustor interface to prevent the combustor flow from traveling into the inlet during certain periods of the operation cycle. Based on how this interface is realized, PDEs can be classified as either valved or valveless, as summarized in Roy et al. [2]. In the valved design, the interface is a mechanical valve located at the head end of the detonation tube [2–4]. The valve is closed during detonation initiation and propagation, as well as the blowdown stage, but remains open during the chamber filling and purging stages [5–11]. The stagnation of the airflow during the valve-closed period leads to some performance loss, although the problem may be mitigated by using multiple detonation tubes [9]. In the valveless design, the isolation between the inlet and the combustor is achieved through gas-dynamic means, such that no valves are required for controlling the air delivery into the combustor [2,12–17]. The system is mechanically simpler and circumvents the disadvantage associated with airflow stagnation in the valved design. The inclusion of a gas-dynamic isolator, however, may considerably limit the engine operation frequency. Until recently, most studies have focused on the flow dynamics and propulsive performance of valved PDEs, with only limited efforts on valveless PDEs.

Presented as Paper 1251 at the 45th AIAA Aerospace Sciences Meeting and Exhibit, Reno Hilton, Reno, Nevada, 8–11 January 2007; received 23 January 2007; revision received 28 November 2007; accepted for publication 1 December 2007. Copyright © 2007 by the authors. Published by the American Institute of Aeronautics and Astronautics, Inc., with permission. Copies of this paper may be made for personal or internal use, on condition that the copier pay the $10.00 per-copy fee to the Copyright Clearance Center, Inc., 222 Rosewood Drive, Danvers, MA 01923; include the code 0748-4658/08 $10.00 in correspondence with the CCC.

*Postdoctoral Research Associate, Department of Mechanical Engineering. Member AIAA.

†Visiting Professor, Department of Mechanical Engineering.

‡John L. and Genevieve H. McCain Chair, Department of Mechanical Engineering; vigor@psu.edu. Fellow AIAA.

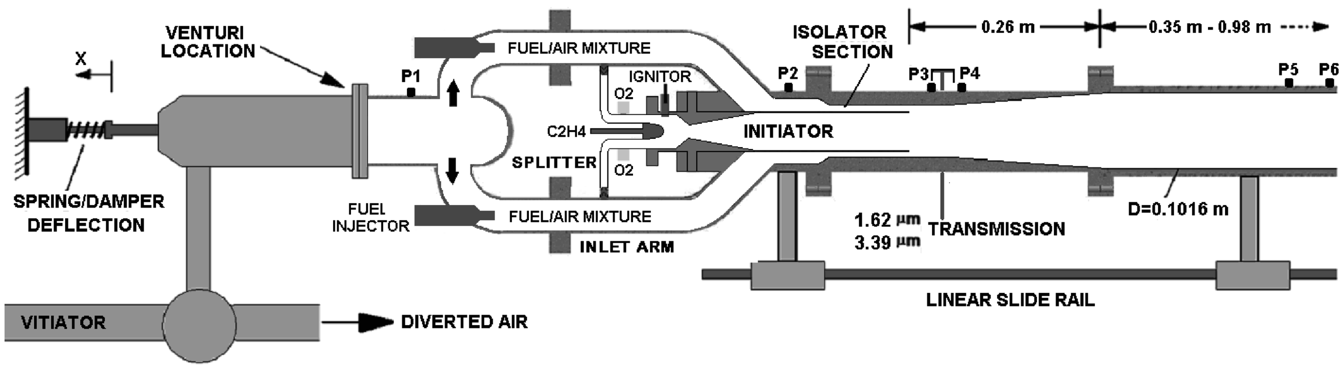

Fig. 1 Schematic of valveless PDE facility [14].

Brophy and colleagues [12–14] conducted a series of experimental studies on valveless PDEs operating on ethylene, propane, and JP-10 fuels. The system, as shown in Fig. 1, uses a coaxial isolator to prevent the upstream propagation of the combustion products and pressure disturbances from the detonation tube to the inlet. An initiator is used for detonation initiation and transmission into the main combustor. The key design issues of this system include successful detonation transmission from the initiator to the combustor, effective isolation between the inlet and the combustor, and reasonable operation frequency. Successful detonation transmission has been demonstrated in multicycle tests operating at frequencies up to 55 Hz, and performance values similar to those of valved PDEs were reported. The effects of fuel distribution on engine operation and performance were also investigated. With a similar design concept, Piton et al. [15] examined PDE operation with hydrogen fuel over a broad range of equivalence ratios. Detonation often collapsed in the transmission zone between the initiator and combustor in cases without obstacles (such as the Schelkine spiral) in this zone, possibly due to the large area expansion from the initiator to the combustor.

In parallel to the experimental investigations [12–14], initial efforts have been applied to study numerically the first cycle of operation with an explicit timing strategy [16,17]. The present work extends our earlier approaches by conducting a comprehensive analysis of the internal flow dynamics in the entire valveless PDEs described in [12–14]. The purposes are to thoroughly understand the various processes in the engine operation, to assess the propulsive performance under limit-cycle conditions, and to provide guidelines for design optimization.

II. System Configuration and Operation

Figure 1 shows schematically the experimental facility described in [14]. The system includes a vitiator, an inlet module, an isolator, an initiator, and a combustor. The hydrogen-fueled vitiator is used to heat the incoming air at a mass flow rate up to 1 kg/s and a temperature up to 550 K to simulate the expected combustor inlet conditions. The inlet module consists of a facility nozzle, four inlet arms, and a common manifold. Fuel injection is controlled by high-speed solenoid valves located on the four inlet arms. The initiator is a 25.4-cm-long tube with an internal diameter of 4.44 cm. It contains a convergent/divergent section near the head end to facilitate mixing and detonation initiation. Injection of fuel and oxygen into the initiator is also controlled by high-speed solenoid valves. A portion of the air/fuel mixture is redirected from the inlet arms to the initiator through the splitter arms using metering orifices and check valves. The isolator has an annular cross section and measures 10.16 cm in length. The combustor consists of a 26.50-cm-long transition section, where the diameter gradually increases from 7.30 to 10.16 cm, and a constant-area section. The entire system is mounted on a linear slide rail on the top of a thrust stand for direct thrust measurement by means of a spring/damper deflection unit. The cycle operation of the system is composed of the following stages, some of which may overlap.

1) Filling of the combustor and initiator with fuel/air mixtures: the fuel injectors on the inlet arms are opened and the resultant fuel/air mixtures are delivered to the combustor and initiator through the inlet arms and the splitter, respectively.

2) Filling of the initiator with an oxygen-enriched fuel/air mixture from the head end by opening the fuel and oxygen valves.

3) Detonation initiation in the initiator and propagation into the combustor: the injection valves in the initiator are closed; the oxygen-enriched mixture is ignited by an ignitor near the head end; a detonation wave is achieved and then transmits to and propagates in the combustor.

4) Exhausting of combustion products and purging of the chamber with air: the fuel injection valves on the inlet arms are closed and air is continuously delivered to the chamber; the detonation wave exits the combustor and a series of rarefaction waves propagates upstream into the combustor and reduces the pressure.

The present configuration and operation sequence represent an improvement over the original version reported in [12]. The initiator and combustor have been shortened to allow for higher operation frequency. The addition of the split flow through the initiator and the corresponding filling strategy prevents the formation of an air plug near the initiator exit that caused the failure of detonation transmission in previous studies [12,16].

The experimental configuration is axisymmetric except for the three-dimensional inlet arms. Consequently, to save computational costs, the present work is based on a two-dimensional axisymmetric analysis. Figure 2 shows the axisymmetric computational domain, which accommodates all the essential elements of the system, including the inlet, isolator, initiator, and combustor. A large external region, measuring 140 cm in length and 70 cm in radius, is also

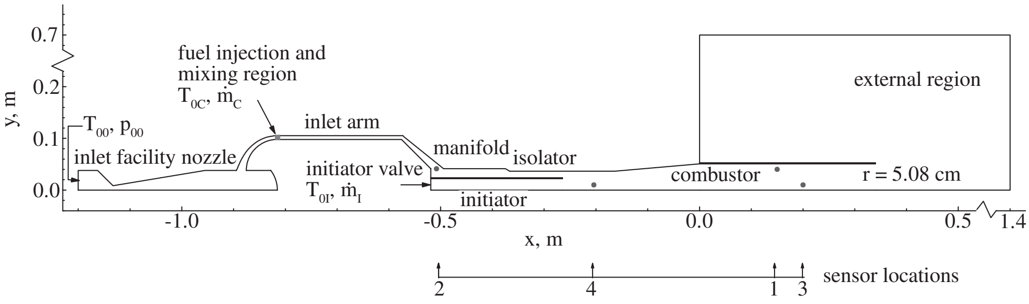

Fig. 2 Computational domain for valveless PDE.

included around the combustor exit plane, to provide a complete description of the flow development and to remove uncertainties in specifying boundary conditions at or near the combustor exit. The origin of the axial coordinate ($x = 0$) is located at the end of the conical section of the combustor. The initiator is a 25.4-cm-long tube with an internal radius of 2.22 cm. The isolator has a length of 10.16 cm, starting from $x = -36.65$ to the initiator exit at -26.49 cm. It has a constant cross-sectional area with a radial span of 1.27 cm. The combustor measures 60.5 cm in length, consisting of a 10.16-cm-long constant-area section with a radius of 3.65 cm, a 16.33-cm-long divergent section with a ramp angle of 5 deg, and another 34.0-cm-long constant-area section with a radius of 5.08 cm. The ratio of the cross-sectional areas of the initiator, isolator, combustor entrance, and combustor exit is 1.00:1.55:2.70:5.22. The radii of the entrance and throat of the inlet facility nozzle are 3.81 and 0.83 cm, respectively. The four inlet arms are approximated as a coaxial channel, whose cross-sectional area remains identical to that of the three-dimensional experimental configuration. For an inviscid flow analysis, the effect of such an approximation on the flow development is expected to be insignificant. The split flow path from the inlet arms to the initiator is not directly simulated, but is treated as a boundary condition at the initiator entrance. The dots represent chemical sensors determining the engine operation timing, which will be discussed in the following paragraphs.

Figure 3 shows the operation time sequence. For simplicity, the valve response time is neglected, that is, the valve is either fully closed or fully open. There are two time lines in the operation, one for the combustor and the other for the initiator. Injection of fuel into the combustor commences at the cycle beginning t_0 and continues for a time period of τ_{fill}. The fuel valve is then closed till the end of the cycle t_5. Starting from the cycle beginning t_0, to simulate the split flow from the inlet arms in experiments, the initiator is charged with air for a time period of τ_{open0}, a fuel/air mixture for a time period of τ_{open1}, and an oxygen-enriched fuel/air mixture for a time period of τ_{open2}. The valve is then closed and ignition is activated at t_4. The valve remains closed till the end of the cycle t_5. In short, the overall PDE operation is controlled by five different time periods: τ_{fill}, τ_{open0}, τ_{open1}, τ_{open2}, and τ_{cycle}.

As in valved PDEs [11], the operation times in the present valveless PDE could be either prespecified (i.e., the external mode) or determined based on local flow conditions (i.e., the internal mode). In our previous study of the first-cycle operation [17], all five time periods were carefully tuned explicitly to achieve successful operation. In practice, it is difficult to obtain a successful limit-cycle operation [8] with this kind of external timing, due to the flowfield deviation from cycle to cycle and the delicate requirement on the timing. For example, when the detonation wave arrives at the initiator exit, the local field should be filled with reactants instead of cold air to achieve successful transmission to the main chamber. To alleviate this problem, in the present work, only the cycle period is explicitly specified, and the other four operation times are implicitly determined by the local flowfield with the aid of four chemical sensors, as denoted by the dots in Fig. 2. The main fuel injector opens at the beginning of each cycle and closes when the fuel/air mixture reaches sensor 1 in the combustor. The filling of a fuel/air mixture in the initiator starts when the fuel/air mixture associated with the main fuel injector reaches sensor 2, and terminates when the fuel/air mixture from the initiator reaches sensor 3 in the combustor. The initiator then fills with an oxygen-enriched fuel/air mixture until the mixture reaches sensor 4. The remaining sequence is identical to that described in the previous paragraph, that is, from time t_4 when the valve is closed and ignition is activated to the end of the cycle t_5.

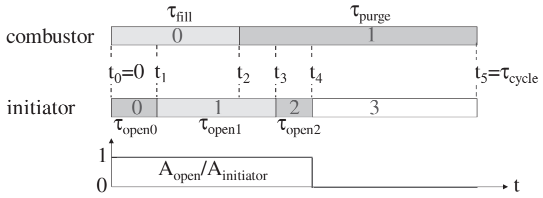

Fig. 3 Operation timing of valveless PDE.

III. Theoretical Formulation and Numerical Framework

A. Governing Equations

The theoretical formulation is based on the variable-property model established in [11]. The analysis accommodates the conservation equations of mass, momentum, energy, and species concentration in axisymmetric coordinates. Diffusive effects are neglected because of their minor roles in determining the overall flow dynamics and propulsive performance of a PDE. The resultant governing equations can be written in the following vector form:

$$\frac{\partial \boldsymbol{Q}}{\partial t} + \frac{\partial \boldsymbol{E}}{\partial x} + \frac{\partial \boldsymbol{F}}{\partial y} = \boldsymbol{H} \tag{1}$$

where the dependent variable vector $\boldsymbol{Q}$, convective flux vectors $\boldsymbol{E}$ and $\boldsymbol{F}$, and source vector $\boldsymbol{H}$ are defined, respectively, as

$$\boldsymbol{Q} = \begin{bmatrix} \rho \\ \rho u \\ \rho v \\ \rho e_t \\ \rho Z_i \end{bmatrix}, \qquad \boldsymbol{E} = \begin{bmatrix} \rho u \\ \rho u^2 + p \\ \rho u v \\ u(\rho e_t + p) \\ \rho u Z_i \end{bmatrix}$$

$$\boldsymbol{F} = \begin{bmatrix} \rho v \\ \rho u v \\ \rho v^2 + p \\ v(\rho e_t + p) \\ \rho v Z_i \end{bmatrix} \tag{2}$$

$$\boldsymbol{H} = \begin{bmatrix} 0 \\ 0 \\ 0 \\ 0 \\ \dot{\omega}_i \end{bmatrix} - \frac{1}{y} \begin{bmatrix} \rho v \\ \rho u v \\ \rho v^2 \\ v(\rho e_t + p) \\ \rho v Z_i \end{bmatrix} + \begin{bmatrix} \dot{m}_s''' \\ \dot{M}_{sx}''' \\ \dot{M}_{sy}''' \\ \dot{E}_s''' \\ \dot{m}_{si}''' \end{bmatrix}$$

Standard notations in gas-dynamics are used, and x and y denote the axial and radial coordinates, respectively. The third term in the source vector $\boldsymbol{H}$ arises from the fuel injection and mixing in the inlet arm, and will be discussed later. The present PDE flowfield involves the fuel (C_2H_4), oxidizers (air and O_2), and resultant detonation products.

Numerical simulations with detailed chemical kinetics and associated species transport for such a system-level analysis would require excessive computational resources. To bypass this difficulty, five nominal species ($i = 1, 5$) are considered herein, namely, stoichiometric C_2H_4/air reactant ($i = 1$) and its detonation product ($i = 2$), stoichiometric C_2H_4/O_2 reactant ($i = 3$) and its detonation product ($i = 4$), and air ($i = 5$). The chemical kinetics for each reactant/product pair ($i1$, $i2$) is modeled by a one-step, irreversible reaction expressed with a single progress variable (i.e., the mass fraction of reactant). The resultant mass production rates of reactant and product become, respectively,

$$\dot{\omega}_{i1} = -\rho Z_{i1} A_{i1} \exp(-T_{ai1}/T) \tag{3}$$

$$\dot{\omega}_{i2} = -(W_{i2}/W_{i1})\dot{\omega}_{i1} \tag{4}$$

The pressure p and temperature T are obtained through the equations of state:

$$p = (\gamma - 1)\rho[e_t - (u^2 + v^2)/2 - Z_1 q_1 - Z_3 q_3] \tag{5}$$

$$T = p/(\rho R) \tag{6}$$

where the gas constant R and specific heat ratio γ of the mixture are calculated, respectively, as the mass-averaged quantities,

$$R = \sum Z_i R_i \tag{7}$$

$$\gamma = \frac{\sum Z_i R_i \gamma_i/(\gamma_i - 1)}{\sum Z_i R_i/(\gamma_i - 1)} \tag{8}$$

with the summation over all the species.

B. Thermophysical and Kinetic Parameters

There are seven model parameters for each reactant/product system: the specific heat ratios and gas constants of reactant and product ($\gamma_{i1}, \gamma_{i2}, R_{i1}, R_{i2}$), the specific heat release of reactant q_{i1}, the preexponential factor A_{i1}, and the activation temperature T_{ai1}. Their values are obtained based on the method described in [11] and summarized in Table 1. The thermophysical parameters ($\gamma_{i1}, \gamma_{i2}, R_{i1}, R_{i2}$, and q_{i1}) are optimized such that the calculated detonation wave speed and Chapman–Jouguet (CJ) properties provide the best match with those predicted by the chemical-equilibrium analysis [18]. The maximum relative errors for the CJ pressure and temperature and detonation wave speed are, respectively, 2, 3, and 1% for the stoichiometric C_2H_4/air mixture, and 4, 5, and 2% for the stoichiometric C_2H_4/O_2 mixture, over the initial pressures of 0.5–2 atm and initial temperatures of 300–500 K. The errors decrease as the initial condition approaches the reference point of 1 atm and 400 K, and are less than 0.5% for most conditions encountered in the present work.

The kinetic parameters (i.e., the preexponential factor A and activation temperature T_a) affect the internal structure of a detonation wave front, but to a much lesser extent, the overall flow evolution. For a system-level analysis of PDEs, it appears unnecessary to resolve the details within a detonation wave front at the expense of excessive computer resources. In light of this, the activation temperature is taken as a common value of 15,100 K, and the preexponential factor is optimized to resolve detonation propagation in the axial direction with a grid size of 1 mm, as described in [11]. It is worth noting that the preexponential factor for the C_2H_4/air mixture is 6 times greater than that for the C_2H_4/O_2 mixture for the current grid system. If the same preexponential factor is used for both mixtures, the grid size for the latter must be much reduced to retain an accurate prediction of detonation propagation, and this could impose severe restrictions on grid resolution.

C. Fuel Injection and Mixing

In the present work, the ethylene fuel (C_2H_4) is not included in the five nominal species and thus cannot be traced separately in the computation. To bypass this problem, the fuel injection is handled along with the mixing process by adding appropriate source terms to the conservation equations. In accordance with the following molar stoichiometric relation among C_2H_4, air, and their stoichiometric mixture C_2H_4/air:

$$C_2H_4 = 15.28\ (C_2H_4/\text{air}) - 14.28\ \text{air} \tag{9}$$

the rate of addition of C_2H_4 can be determined by those of the stoichiometric C_2H_4/air mixture and air, respectively,

$$\dot{m}'''_{s1} = \dot{m}'''_{C_2H_4/\text{air}} = \dot{m}'''_{C_2H_4} \times 15.28 W_{C_2H_4/\text{air}}/W_{C_2H_4} \tag{10}$$

$$\dot{m}'''_{s5} = \dot{m}'''_{\text{air}} = -\dot{m}'''_{C_2H_4} \times 14.28 W_{\text{air}}/W_{C_2H_4} \tag{11}$$

The source term arising from the fuel addition in the mass conservation Eq. (1) becomes

$$\dot{m}'''_s = \dot{m}'''_{C_2H_4} \tag{12}$$

For axial, sonic injection, the rates of momentum and energy addition can be expressed as

$$\dot{M}'''_{sx} = \dot{m}'''_s \sqrt{T_{0C}[2R\gamma/(\gamma+1)]_{C_2H_4}} \tag{13}$$

$$\begin{aligned} \dot{E}'''_s = \dot{m}'''_s \{ & T_{0C}[R\gamma/(\gamma-1)]_{C_2H_4} \\ & + q_{C_2H_4/\text{air}} \times 15.28 W_{C_2H_4/\text{air}}/W_{C_2H_4} \} \end{aligned} \tag{14}$$

where the gas constant and specific heat ratio of C_2H_4 can be calculated from Eqs. (7) and (8), respectively, with the mass fraction Z obtained from Eq. (9). The volumetric mass addition rate of fuel, $\dot{m}'''_{C_2H_4}$, in the injection and mixing region can be specified empirically. For simplicity, a uniform distribution is employed herein such that

$$\dot{m}'''_{C_2H_4} = \dot{m}_C/V \tag{15}$$

In the present study, the injection and mixing take place within the inlet arm from $x = -81.5$ to -80.5 cm, as indicated in Fig. 2. The total temperature and mass injection rate of the fuel (T_{0C} and $\dot{m}_C$) are treated as input parameters.

D. Mole Fraction Conversion from Constituent to Nominal Species

For a given mixture composition, the mole fractions of C_2H_4, N_2, and O_2 can be determined by the corresponding values of the nominal species of air and stoichiometric mixtures C_2H_4/air and C_2H_4/O_2:

$$\begin{aligned} & a_1(C_2H_4/\text{air}) + a_2(C_2H_4/O_2) + a_3(\text{air}) \\ & \quad = b_1(C_2H_4) + b_2(O_2) + b_3(N_2) \end{aligned} \tag{16}$$

The relation between coefficients a and b can be easily obtained from the conservation of atoms. As a specific example, the oxygen-enriched C_2H_4/air mixture delivered to the initiator, which has mole fractions of 0.197 (C_2H_4), 0.592 (N_2), and 0.210 (O_2), is equivalent to a mixture of C_2H_4/air and C_2H_4/O_2 with mole fractions of 0.285 and 0.715, respectively, or mass fractions of 0.271 and 0.729.

E. Boundary Conditions and Detonation Initiation

The boundary conditions at the head end of the initiator are specified according to the desired flow properties at each stage of engine operation. The head end is modeled as a rigid wall during the valve-closed stage. When the valve is open, the total temperature (T_{0I}), mass flow rate ($\dot{m}_I$), and species mass fractions of the filling gas are specified. The axial velocity is extrapolated from the interior points. All the solid walls are assumed to be adiabatic. The radial velocity and normal gradients of the axial velocity, pressure, temperature, and species mass fractions are set to zero at the centerline because of flow symmetry. Along the open boundary of the external region, either a zero-gradient or a fixed-pressure condition can be implemented. Numerical experiments have revealed that these two conditions lead to almost identical results

Table 1 Model parameters for the $C_2H_4/\text{air}/O_2$ system

	γ_{i1}	R_{i1}, J/kg · K	γ_{i2}	R_{i2}, J/kg · K	q_{i1}, MJ/kg	T_{ai1}, K	A_{i1}, 1/s
C_2H_4/air ($i1 = 1$, $i2 = 2$)	1.3681	287.62	1.1585	297.67	4.8281	15,100	3.0×10^8
C_2H_4/O_2 ($i1 = 3$, $i2 = 4$)	1.3020	268.08	1.1374	369.48	9.4634	15,100	5.0×10^7
Air ($i1 = 5$)	1.4	287.00	——	——	——	——	——

in terms of the engine internal flow evolution and propulsive performance, if the external region is sufficiently large. Detonation is directly initiated at the head end by raising the local gas temperature and pressure to sufficiently high values over a small spatial domain.

F. Numerical Method

The theoretical formulation outlined previously is solved numerically using the space-time conservation element/solution element method described in [19,20]. The scheme offers such advantages as a unified treatment of space and time, introduction of solution and conservation elements to construct a simple stencil, treatment of dependent variables and their derivatives as unknowns to be solved simultaneously, and no interpolation or extrapolation required to evaluate fluxes at cell interfaces. Furthermore, it has extremely low numerical dissipation and dispersion errors, and is thus very effective in treating detonation waves and shock discontinuities. The resultant computer code is further parallelized using the message-passing-interface library and a domain-decomposition technique for unstructured grids [21].

The entire computational domain shown in Fig. 2 is discretized into 166,743 unstructured triangular grid cells, of which 124,768 are located in the internal region and 41,975 in the external region. The grid cell size is about 0.1 cm within the internal region, and increases to 2.0 cm near the upper right corner of the external region. A total of 52 numerical point probes and four planar probes are employed in various parts of the system to monitor the flowfield evolution. The current grid is not intended to resolve detailed structures of a detonation wave front [22], which would require a much finer grid not practical nor necessary for a system-level analysis of PDE dynamics and performance. A grid-independence analysis was conducted by refining the spatial resolution by a factor of 2 in both the axial and radial directions to ensure numerical accuracy. Results show almost identical flow evolution and detonation dynamics, with pressure signals differing by less than 1% between the baseline- and fine-grid solutions in the bulk of the computed engine flowfield. This simple grid-independence analysis is thus sufficient for the current problem, although a more general and strict study may be conducted based on the Richardson extrapolation or the grid convergence index methodologies [23,24].

IV. Results and Discussion

A. Cold-Flow Development

The gas dynamics over the entire engine flowpath were first studied by charging the system for a sufficient time period. The results obtained provided the initial condition for full-cycle simulations. The total pressure and total temperature at the inlet entrance are set to the experimental values of 13.93 atm and 430 K, respectively. The corresponding air mass flow rate is 0.56 kg/s. The total temperature at the initiator entrance is 430 K, and the injected mass flow rate is fixed at 0.3 kg/s. All the fuel injectors are closed. The entire domain is initially filled with stagnant air at 1 atm and 300 K. The flow attains its steady state in about 30 ms.

Figure 4 shows the Mach-number distribution in the entire field, along with close-up views of the flow development in the facility nozzle and the upstream regions of the initiator and isolator. Within the nozzle, a strong shock of Mach number 4.1 is stabilized in the divergent section, and causes the total pressure to decrease significantly from 13.93 to 1.65 atm. The shock acts as an effective acoustic damper, absorbing disturbances arising from the downstream region [25,26]. The flow distribution along the centerline of the nozzle closely matches that calculated using a quasi-one-dimensional analysis [17]. The Mach number in the manifold is about 0.44. The flow accelerates through the convergent section at the end of the manifold, and becomes slightly supersonic near the isolator entrance, as indicated by the sonic line in Fig. 4c. The Mach number within the isolator reaches 0.91. Such a transonic flow provides gas-dynamic isolation of the inlet from the combustor and contributes to reasonable system performance by avoiding the occurrence of shocks in a supersonic flow. If a smaller isolator is employed, the flow may become supersonic and a shock forms near the initiator exit [16]. The axial flow velocities at the exits of the initiator and isolator are 290 and 350 m/s, respectively.

The effect of the initiator mass injection rate was investigated. Figure 5 shows the velocity fields and streamlines in the combustor. For a mass injection rate of 0.1 kg/s, the axial flow velocities at the exits of the initiator and isolator are 70 and 240 m/s, respectively. The large velocity disparity gives rise to the development of a recirculation zone in the combustor. As the mass injection rate increases, both stream velocities increase, but the difference between them decreases, which causes the recirculation zone to weaken and move downstream. At a mass injection rate of 0.3 kg/s, the flow

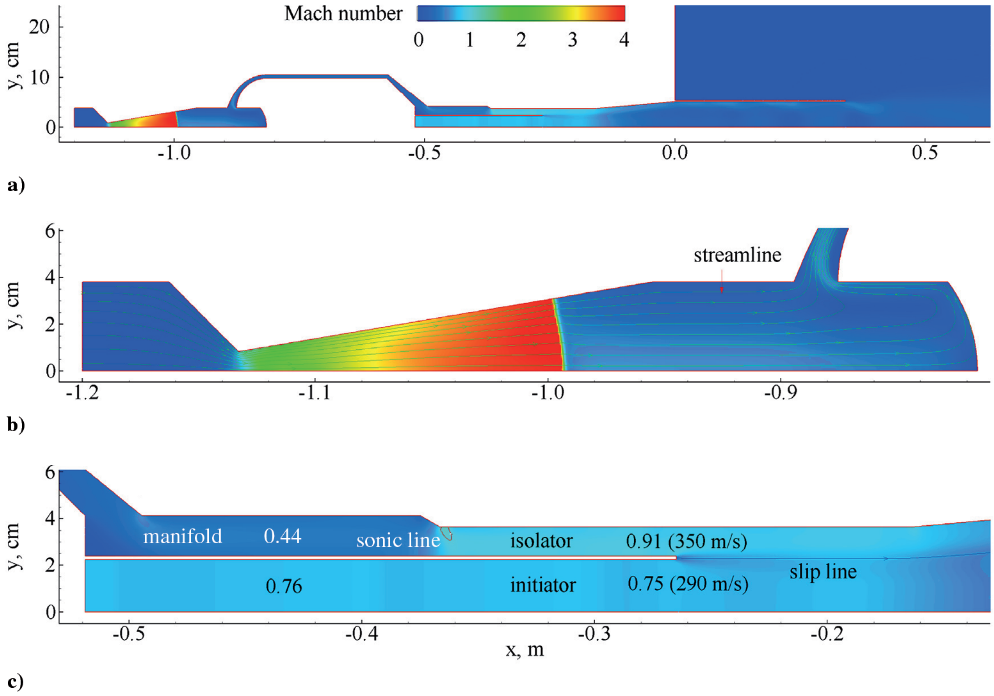

Fig. 4 Cold flowfield with initiator mass flow rate of 0.3 kg/s.

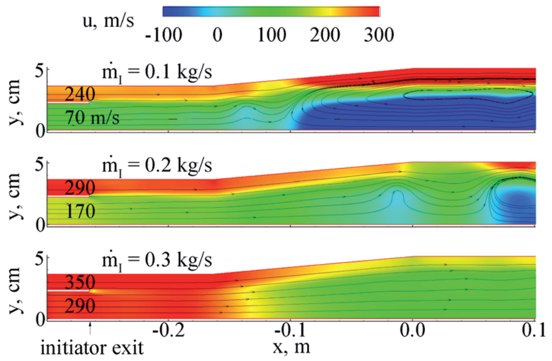

Fig. 5 Effect of initiator mass flow rate on cold-flow development.

becomes more uniform and no recirculation zone is observed in the combustor.

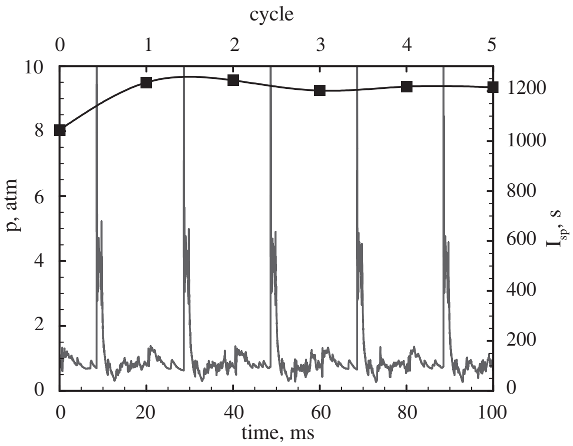

Fig. 6 Time history of pressure at 5.08 cm downstream of initiator exit and specific impulse during five continuous cycles.

B. Limit-Cycle Operation

1. *Flow Evolution*

The cold flowfield established above is used as the initial condition for a full-cycle operation. Table 2 summarizes the operating conditions for the baseline case, simulating the experiments conducted by Brophy and colleagues [12–14]. The total pressure and total temperature at the entrance of the facility nozzle are 13.93 atm and 430 K, respectively. The mass flow rate of the fuel injected into the combustor is set to 0.038 kg/s, rendering a stoichiometric C_2H_4/air mixture. The total temperature of the fuel is chosen to be the experimental value of 300 K. For the initiator, the mass injection rate is fixed at 0.3 kg/s, and the total temperature at the entrance is 430 K. The initiator is charged during different stages with air, a stoichiometric C_2H_4/air mixture, and a combination of a stoichiometric C_2H_4/air mixture and a stoichiometric C_2H_4/O_2 mixture with their respective mass fractions of 0.271 and 0.729. The operation cycle period is set to 20 ms. The four sensors for operation control are located, respectively, near the upper wall (15.0, 4.00) and the centerline (20.0, 1.00) of the combustor, at the exit of the inlet arm (−50.6, 4.13), and near the initiator exit (−21.4, 0.00) cm, as shown by the solid dots in Fig. 2. Calculations are carried out for a time period sufficient to ensure the attainment of a steady cyclic operation. Figure 6 shows the time history of pressure at 5.08 cm downstream of the initiator exit and specific impulse. It takes about five cycles for the baseline case to reach a limit-cycle condition, and the corresponding τ_{fill}, τ_{open0}, τ_{open1}, and τ_{open2} are 6.63, 3.10, 4.18, and 1.14 ms, respectively.

Figure 7 shows the time evolution of the C_2H_4/air mass-fraction field (Z_1) during a limit cycle. The corresponding time histories at different probes are given in Fig. 8. At the beginning of each cycle (Fig. 7a), the system is filled with air, and no reactant is present in the flowfield. The C_2H_4 fuel is injected through the main injectors, forming a stoichiometric C_2H_4/air reactant stream within the inlet arm. The C_2H_4/air mixture mass fraction at the injector increases to about 1.0 (Fig. 8, probe 14). At $t = 3.10$ ms, the leading fresh reactant reaches sensor 2, located at the end of the inlet arm, and the initiator starts charging with the C_2H_4/air mixture (Fig. 7b). The C_2H_4/air mixture mass fraction jumps from 0 to 1.0 (Fig. 8, probe 24). At $t = 4.4$ ms, the upper reactant stream approaches the isolator exit, while the lower stream has already passed the initiator exit, as shown in Fig. 7c. The corresponding axial velocities at the isolator and initiator exits are 330 and 297 m/s, respectively. In an ideal situation, the two reactant streams should reach the isolator and initiator exits simultaneously and with the same axial velocity. In the present baseline case, their corresponding arrival times are 4.45 and 4.23 ms, respectively, as indicated by the time histories at probes 23 and 26 in Fig. 8.

At $t = 6.63$ ms, the upper reactant stream reaches sensor 1 in the combustor, and the main fuel injector closes (Fig. 7d). The two reactant streams merge and continue to travel downstream in the combustor. At $t = 7.28$ ms, the lower reactant stream reaches sensor 3 near the combustor centerline, and the initiator begins filling with an oxygen-enriched C_2H_4/air mixture, as shown in Fig. 7e and also indicated by the sudden decrease of Z_1 from 1.0 to 0.271 at probe 24. The filling gas velocity at the initiator head end is about 270 m/s. At $t = 8.42$ ms, the C_2H_4/air/O_2 mixture reaches sensor 4 located at 5.08 cm downstream of the initiator exit (Fig. 7f). The overfilling of the initiator is expected to facilitate detonation transmission. The initiator valve then closes and the detonation is directly initiated by a small amount of high-temperature and high-pressure driver gas spanning 0.08 cm from the head end. It is also observed in Fig. 7f that some reactants have spilled out of the combustor. At $t = 8.5$ ms, the detonation wave is about to reach the initiator exit, while the downward part of the inlet arm is still filled with reactants (Fig. 7g). In an ideal situation, the detonation wave should reach the initiator exit slightly before the arrival of the trailing edge of the upper reactant stream at the isolator exit. In the present case, the detonation wave arrives at the initiator exit at 8.53 ms, as

Table 2 Full-cycle operation of baseline case

Inlet condition	Total temperate T_{00}	430 K
	Total pressure p_{00}	13.93 atm ($\Rightarrow$ 0.56 kg/s mass flow rate)
Main combustor injection	Total temperate T_{0C}	300 K
	Mass injection rate $\dot{m}_C$	0.038 kg/s ($\Rightarrow$ equivalence ratio1.0)
Initiator injection	Total temperate T_{0I}	400 K
	Mass injection rate $\dot{m}_I$	0.3 kg/s
	Mass fractions Z_{open1}	1.0 (C_2H_4/air)
	Mass fractions Z_{open2}	0.271 (C_2H_4/air) + 0.729 (C_2H_4/O_2)
Operation timing	τ_{cycle}	20 ms
	Sensor 1 location	(15, 4.00) cm ($\Rightarrow \tau_{\text{fill}} = 6.63$ ms)
	Sensor 2 location	(−50.6, 4.13) cm ($\Rightarrow \tau_{\text{open0}} = 3.10$ ms)
	Sensor 3 location	(20.0, 1.00) cm ($\Rightarrow \tau_{\text{open1}} = 4.18$ ms)
	Sensor 4 location	(−21.4, 0.00) cm ($\Rightarrow \tau_{\text{open2}} = 1.14$ ms)

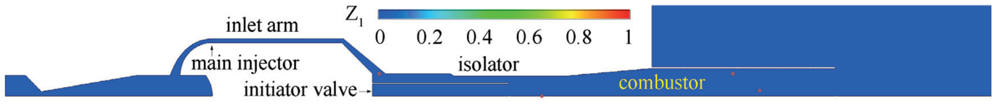

a) t=0 ms cycle begins

b) t=3.2 ms initiator begins filling with C_2H_4/air

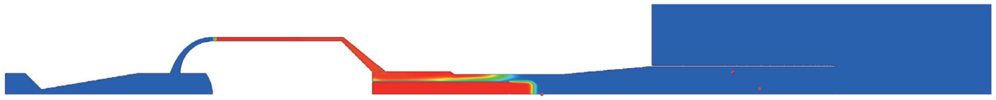

c) t=4.4 ms

d) t=6.7 ms main injector closes

e) t=7.4 ms initiator begins filling with C_2H_4/air/O_2

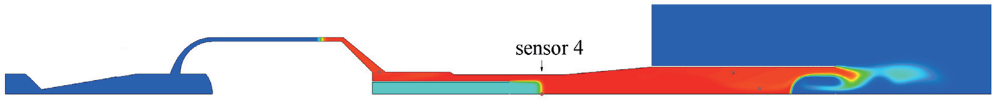

f) t=8.4 ms initiator filling ends

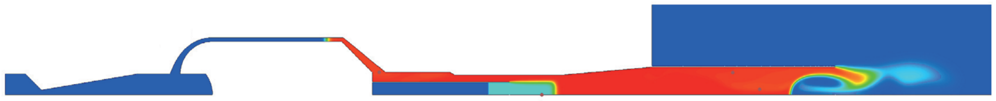

g) t=8.5 ms detonation propagates in initiator

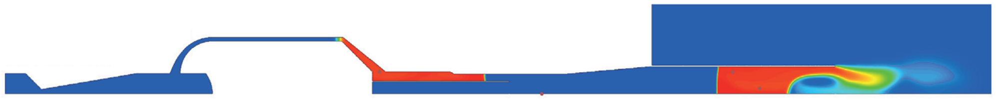

h) t=8.7 ms detonation propagates in combustor

Fig. 7 Time evolution of C_2H_4/air mixture mass fraction during a limit cycle for a baseline case; $\tau_{\text{cycle}} = 20$ ms.

indicated by the time history of Z_1 at probe 26. The detonation wave then successfully transmits to the combustor, leaving a decoupled shock and deflagration wave propagating upstream in the isolator (Fig. 7h). At $t = 8.81$ ms, the detonation wave reaches the combustor exit. The flow evolution in the chamber is then characterized by a blowdown process until the end of the cycle at 20 ms. It is worth noting that a small amount of reactant remains unburned in the inlet arm during the blowdown process. It first moves

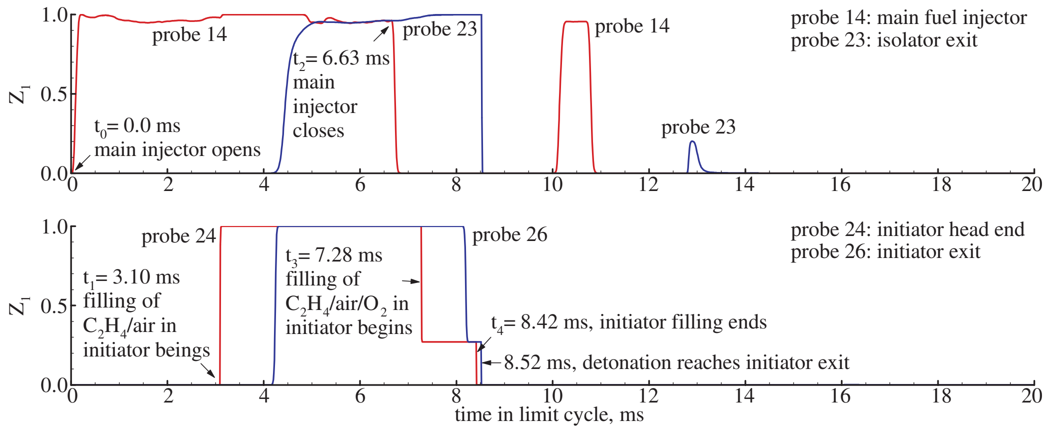

Fig. 8 Time histories of C_2H_4/air mixture mass fraction at different probe locations during a limit cycle for a baseline case.

upstream with the shock wave and is later pulled downstream by expansion waves. As a consequence, the mass fraction of the C_2H_4/air mixture reaches 1.0 at probe 14 during 10.1–10.8 ms, as indicated in Fig. 8.

Figure 9 shows the temporal evolution of the pressure field in the engine facility, permitting further exploration of the flow development and detonation wave dynamics. Once the detonation exits the initiator and propagates downstream, the Mach reflection of the leading shock on the chamber wall generates a high-pressure region and reinforces the detonation transmission into the combustor. Figure 10 shows a close-up view of the process. At $t = 8.52$ ms, the detonation wave leaves the initiator, and a series of expansion waves form at the trailing edge of the initiator wall and subsequently affect the evolution of the detonation/shock wave. In the strongly diffracted region near the wall, the detonation wave degenerates to a curved shock decoupled from the combustion wave (Fig. 10b). The leftmost part of the shock propagates upstream into the isolator. The remaining shock hits and reflects from the upper wall, creating a region of elevated pressure and temperature between the wall and shock to ignite the local unburned reactants. The transverse shock wave proceeds further downward and reflects off the symmetry boundary (Fig. 10f). From $t = 8.58$ to 8.63 ms, the Mach reflection point and the associated high-temperature and high-pressure regions move toward and finally catch up with the detonation wave front. The detonation transmission process is thus reinforced. The successful detonation propagation in the combustor is also evidenced by the time histories of pressure at different locations shown in Fig. 11. The maximum pressure at probes 38 and 44 reaches about 16 atm, whereas the CJ pressure is about 12 atm. The corresponding detonation wave speed is 2000 m/s, matching the CJ detonation velocity.

A grid-independence analysis was conducted for the detonation transmission by using another two different grids. The baseline grid size (0.1 cm) was either doubled to 0.2 cm or refined to 0.05 cm. The results from both grids exhibit almost identical flow evolution shown in Fig. 10. The snapshots of the pressure field at $t = 8.6$ ms are plotted in Fig. 12. A more quantitative comparison is given in Fig. 13 based on the time history of pressure at $x = -16.3$ cm (the entrance of the divergent section). The time-averaged pressures over a time period from 8.5 to 10 ms are 3.45, 3.40, and 3.40 atm for the coarse, baseline, and fine grids, respectively. It is worth noting that the current grids are not fine enough to resolve the cellular structures and other details within the detonation wave front [22], which play a significant role in dictating detonation diffraction and reinitiation

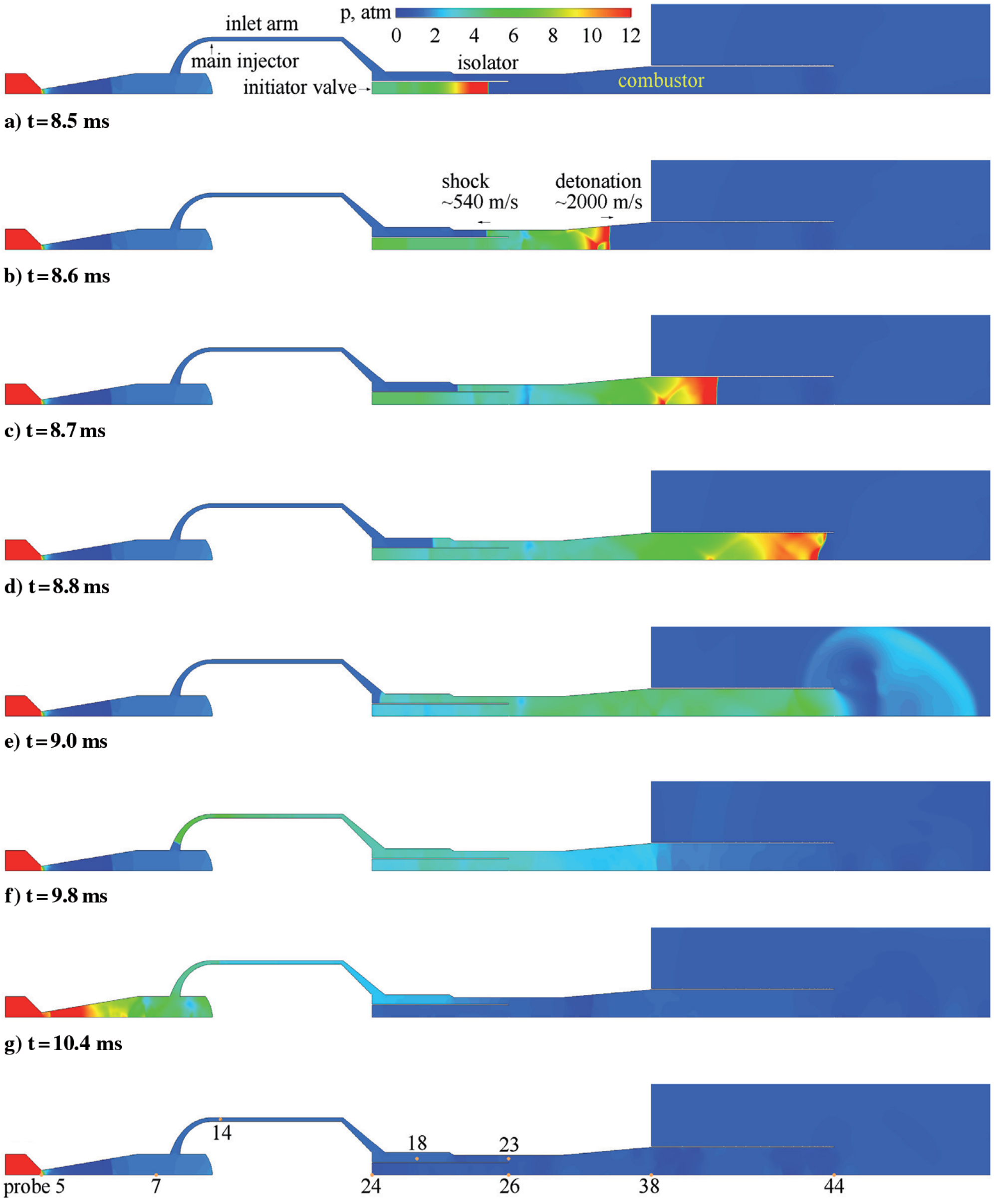

a) t = 8.5 ms

b) t = 8.6 ms

c) t = 8.7 ms

d) t = 8.8 ms

e) t = 9.0 ms

f) t = 9.8 ms

g) t = 10.4 ms

h) t = 20.0 ms

Fig. 9 Time evolution of pressure field during a limit cycle for a baseline case.

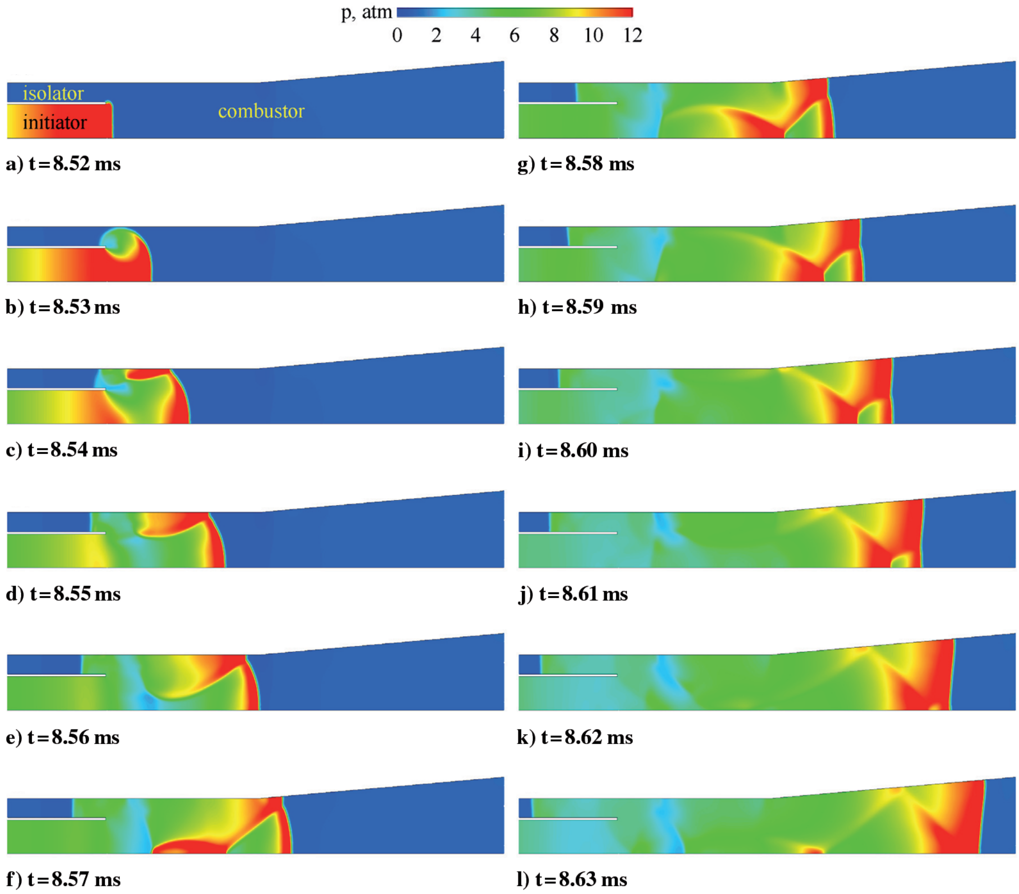

a) t=8.52 ms
g) t=8.58 ms
b) t=8.53 ms
h) t=8.59 ms
c) t=8.54 ms
i) t=8.60 ms
d) t=8.55 ms
j) t=8.61 ms
e) t=8.56 ms
k) t=8.62 ms
f) t=8.57 ms
l) t=8.63 ms

Fig. 10 Close-up view of time evolution of pressure field during detonation transmission from initiator to combustor.

(during a very short period of an operation cycle). Such phenomena can be handled with a much finer grid [22].

Within the isolator, the shock wave propagates upstream at a speed of 540 m/s, followed by a combustion wave at 240 m/s (Fig. 9b). Severe flow reversal occurs behind the shock, although the flow is nearly sonic in front of it. At $t = 9.03$ ms, the shock wave reaches the inlet arm (Fig. 9e) and is bounced off by the head end of the manifold. The reflected shock travels downstream and returns the flow to positive velocity. The phenomenon is further examined in Fig. 14, which shows the time histories of the Mach number and axial flow velocity at the middle of the isolator ($x = -31.5$ cm). The flow velocity is initially nearly sonic. It decreases abruptly to a negative value when the shock wave arrives at 8.6 ms, and then becomes positive when the reflected shock arrives at 9.5 ms.

Figures 9f and 9g show the propagation of the shock wave through the inlet arm and the facility nozzle, respectively. The stationary shock originally located in the divergent section of the facility nozzle acts as an effective damper, absorbing disturbances from the downstream region. As a consequence, the upstream-running shock wave from the inlet arm and the resultant flow disturbances are dissipated rapidly. The entire flowfield then returns to its initial state at the commencement of each cycle (Fig. 9h). During the blowdown process, the pressure near the main fuel injector (probe 14 in Fig. 11) may reach a maximum of 7 atm, much higher than the value of 1.5 atm, which is reached during the chamber-filling stage. To enhance the isolation effect and reduce flow oscillations in the inlet, the amount of reactant in the isolator should be minimized when the detonation wave exits the initiator. This can be achieved by optimizing the engine operation timing and by using a longer isolator. In an ideal situation, the expansion waves, formed when the detonation wave exits the combustor, should catch up with the upstream-traveling shock wave in the isolator to substantially reduce the shock strength.

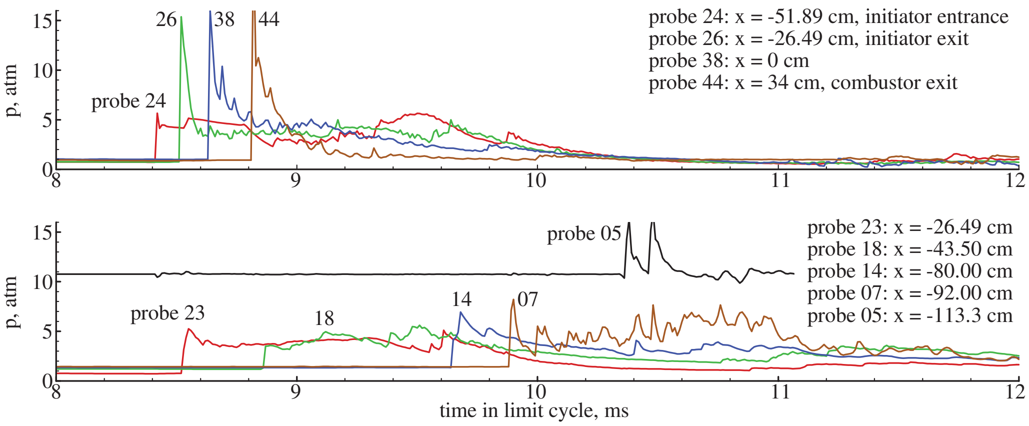

Fig. 11 Time histories of pressure at different probe locations during a limit cycle for a baseline case.

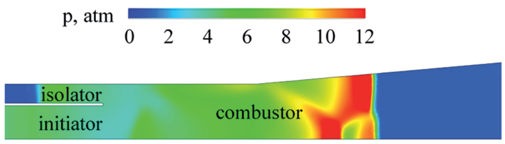

a) Coarse grid (0.2 cm)

b) Baseline grid (0.1 cm)

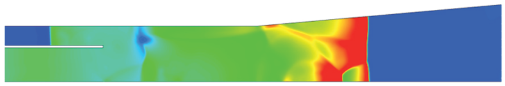

c) Fine grid (0.05 cm)

Fig. 12 Snapshots of pressure field at $t = 8.6$ ms (in limit cycle) for coarse, baseline, and fine grids.

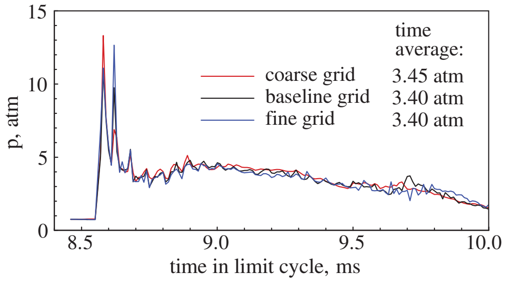

Fig. 13 Time histories of pressure at entrance of divergent section ($x = -16.3$ cm) during a limit cycle for coarse, baseline, and fine grids.

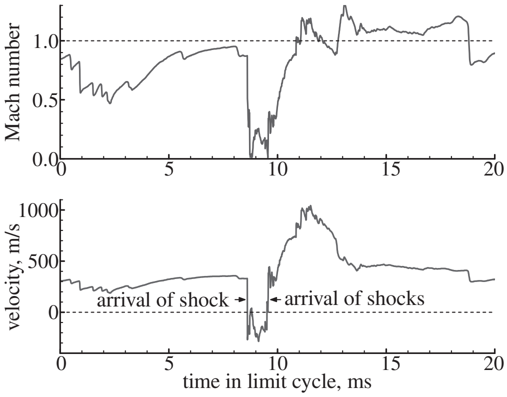

Fig. 14 Time history of Mach number at middle of isolator ($x = -31.5$ cm) during a limit cycle for a baseline case.

The calculated time history of the wall pressure at 5.08 cm downstream of the initiator exit was compared with experimental data [13]. The good agreement shown in Fig. 15 suggests the validity of the present approach. The pressure spike at 8.55 ms results from the arrival of the detonation wave. A plateau period of around 1 ms then occurs, followed by a gradual decrease of pressure during the blowdown process. Figure 16 shows the time evolution of the area-averaged temperature on the transverse plane at the same axial location. As a reference, the CJ temperatures of the stoichiometric C_2H_4/air and C_2H_4/O_2 mixtures are about 3000 and 4000 K, respectively.

2. *Propulsive Performance*

The instantaneous gross thrust can be determined based on the flow properties at the combustor exit plane as follows [11]:

$$F^g = \dot{m}_e u_e + (p_e - p_b)A \tag{17}$$

where the mass flow rate $\dot{m}_e$, velocity u_e, and pressure p_e are spatially averaged over the transverse plane. Figure 17 shows the time evolution of the thrust during a limit cycle. Also included is the instantaneous force at $x = -92$ cm in the inlet facility nozzle. The large spike in each cycle corresponds to the arrival of the detonation or primary shock wave at the exit plane. The cycle-averaged gross thrust $\bar{F}^g$ reaches a stationary value of 349 N in the limit cycle. The gross specific impulse is obtained as

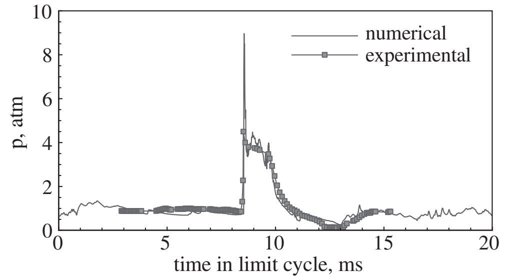

Fig. 15 Comparison with experimental results [13] for wall pressure at 5.08 cm downstream of initiator exit during a limit cycle.

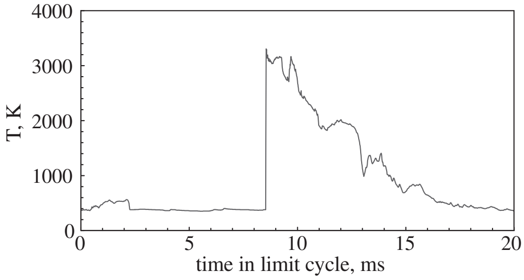

Fig. 16 Time history of area-averaged temperature over a transverse plane at 5.08 cm downstream of initiator exit during a limit cycle for a baseline case.

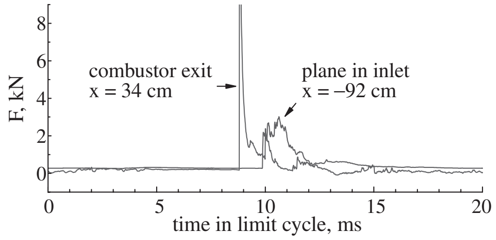

Fig. 17 Instantaneous forces at $x = 34$ cm (combustor exit plane) and $x = -92$ cm (inlet arm) during a limit cycle for a baseline case.

$$I_{\mathrm{sp}}^g = \frac{\bar{F}^g \times \tau_{\mathrm{cycle}}}{(m_{C_2H_4} + m_{O_2})g} = 1215 \text{ s} \tag{18}$$

where the amounts of air, C_2H_4, and oxygen delivered to the system during each limit cycle are summarized in Table 3. The calculated I_{sp}^g agrees well with the experimentally measured value of 1200 s [14]. The net thrust and net specific impulse of the facility can be

Table 3 C_2H_4, air, and oxygen mass delivered to the system during each limit cycle

	Combustor	Initiator	Total
Air, g	11.2	2.19	13.4
C_2H_4, g	0.25	0.14	0.39
O_2, g	0	0.19	0.19

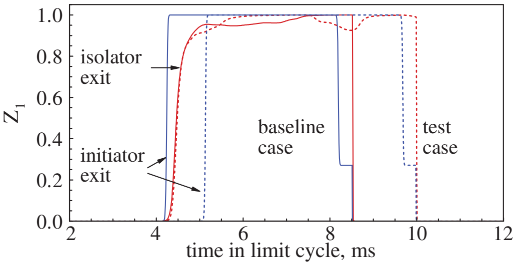

Fig. 18 Time histories of C_2H_4/air mixture mass fraction at isolator and initiator exits for two different locations of sensor 2: $x = -50.6$ cm for the baseline case and $x = -36.7$ cm for the test case.

determined by subtracting the momentum and pressure forces of the incoming air from Eq. (17).

In practice, the specific impulse can be improved by minimizing the amount of oxygen required for successful detonation initiation and transmission to the combustor. Also, an exhaust nozzle for the combustor is needed to enhance the engine performance by preserving the chamber pressure during the blowdown stage and increasing the reactant loading density during the filling stage [11].

C. Effect of Operation Timing

The effect of operation timing on the internal flow evolution was investigated by varying the locations of the chemical sensors. Figure 18 shows the time histories of the C_2H_4/air mixture mass fraction at the isolator and initiator exits for two different locations of sensor 2: $x = -50.6$ cm for the baseline case and $x = -36.7$ cm for the test case. In the baseline case, the lower reactant stream reaches the initiator exit at 0.22 ms before the upper reactant stream arrives at the isolator exit. The situation is reversed for the test case, in which the lower stream arrives at 0.65 ms later than the upper stream. The change in the location of sensor 2 mainly affects the time lag between the upper and lower reactant streams. The effect amounts to the variation of the operation timing associated with sensor 2: the initiator starts the filling of reactants when the upper stream reaches sensor 2. Similarly, sensors 1 and 3 determine the fraction of the combustor that is filled with reactants, and sensor 4 controls the amount of the oxygen-enriched C_2H_4/air mixture delivered to the initiator.

Compared with a valved PDE [11], the valveless PDE requires a more careful control of the operation timing; the detonation transmission from the inlet to the combustor, fuel spillage from the combustor, and amount of fuel residue in the inlet appear to be quite sensitive to timing. Figure 19 shows snapshots of the C_2H_4/air mass-fraction and pressure fields for a failure case, in which sensor 1 is moved to 10 cm from $x = 15$ cm of the baseline case. At $t = 91.7$ ms, the detonation wave is still propagating through the initiator. The trailing edge of the upper reactant stream, however, has moved farther downstream of the isolator, and the region near the isolator exit is filled with air. As a consequence, a strong expansion occurs when the detonation wave emerges from the initiator, causing the failure of detonation transmission into the combustor. This phenomenon can be further elucidated by the mass-fraction and pressure fields at 71.5 ms. At this instant, the leading shock wave has reached $x = 20$ cm, whereas the reaction front has arrived only at $x = 12$ cm. Further, the pressure behind the shock is only 4 atm, much less than the CJ pressure of 12 atm. The detonation wave has degenerated to a shock wave decoupled from the combustion zone. Also observed in this case is the considerable spillage of reactants in the upper stream out of the combustor.

V. Conclusions

A numerical framework has been established to investigate the internal flow dynamics and to assess the propulsive performance of an airbreathing valveless pulse detonation combustor using ethylene as fuel. The model treats the full conservation equations in axisymmetric coordinates and accommodates finite-rate chemistry and variable thermophysical properties. The cold-flow development in the entire system was first studied. Results indicated that the mass flow rates in the main chamber and initiator need to be carefully tuned to provide effective gas-dynamic isolation of the combustor from the inlet and to avoid the occurrence of flow recirculation in the combustor. The detailed flow evolution and detonation wave dynamics during a limit-cycle operation were then explored. Successful detonation transmission from the initiator filled with an oxygen-enriched C_2H_4/air mixture to the combustor filled with a stoichiometric C_2H_4/air mixture was demonstrated. The calculated pressure histories and gross specific impulse of 1215 s show good agreement with experimental results. The effect of operation timing was also examined to help explore the flow sensitivity and to identify design attributes for improving the system performance.

Acknowledgments

This work was supported by the Office of Naval Research under Grant No. N00014-05-1-0159. The support and encouragement of Gabriel Roy are gratefully acknowledged. The authors are also grateful to Christopher Brophy for providing experimental details and technical advice.

References

[1] Kailasanath, K., “Recent Developments in the Research on Pulse Detonation Engines,” *AIAA Journal*, Vol. 41, No. 2, 2003, pp. 145–159.

[2] Roy, G. D., Frolov, S. M., Borisov, A. A., and Netzer, D. W., “Pulse Detonation Propulsion: Challenges, Current Status, and Future Perspective,” *Progress in Energy and Combustion Science*, Vol. 30, No. 6, 2004, pp. 545–672.
doi:10.1016/j.pecs.2004.05.001

[3] Schauer, F., Stutrud, J., and Bradley, R., “Detonation Initiation Studies and Performance Results for Pulsed Detonation Engine Applications,” AIAA Paper 2001-1129, Jan. 2001.

[4] Bussing, T. R. A., Lidstone, G. L., Christofferson, E., Kaemming, T. A., and Jones, G., “Pulse Detonation Propulsion Proof of Concept Test Article Development,” AIAA Paper 2002-3633, July 2002.

[5] Cambier, J. L., and Tegner, J. K., “Strategies for Pulsed Detonation Engine Performance Optimization,” *Journal of Propulsion and Power*, Vol. 14, No. 4, 1998, pp. 489–498.

[6] Yungster, S., “Analysis of Nozzle Effects on Pulse Detonation Engine Performance,” AIAA Paper 2003-1316, Jan. 2003.

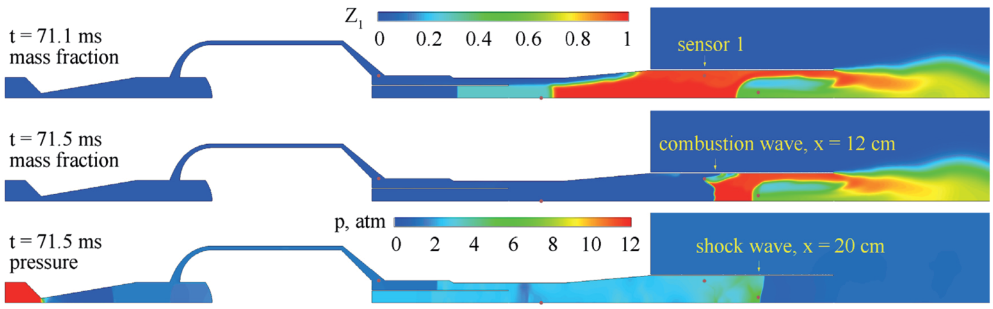

Fig. 19 Snapshots of C_2H_4/air mass-fraction and pressure fields for a failure case with sensor 1 moved upstream from 15 to 10 cm.

[7] Wu, Y. H., Ma, F. H., and Yang, V., "System Performance and Thermodynamic Cycle Analysis of Airbreathing Pulse Detonation Engines," *Journal of Propulsion and Power*, Vol. 19, No. 4, 2003, pp. 556–567.

[8] Ma, F. H., Choi, J. Y., and Yang, V., "Thrust Chamber Dynamics and Propulsive Performance of Single-Tube Pulse Detonation Engines," *Journal of Propulsion and Power*, Vol. 21, No. 3, 2005, pp. 512–526.

[9] Ma, F. H., Choi, J. Y., and Yang, V., "Thrust Chamber Dynamics and Propulsive Performance of Multitube Pulse Detonation Engines," *Journal of Propulsion and Power*, Vol. 21, No. 4, 2005, pp. 681–691.

[10] Harris, P. G., Stowe, R. A., Ripley, R. C., and Guzik, S. M., "Pulse Detonation Engine as a Ramjet Replacement," *Journal of Propulsion and Power*, Vol. 22, No. 2, 2006, pp. 462–473.

[11] Ma, F. H., Choi, J. Y., and Yang, V., "Propulsive Performance of Airbreathing Pulse Detonation Engines," *Journal of Propulsion and Power*, Vol. 22, No. 6, 2006, pp. 1188–1203. doi:10.2514/1.21755

[12] Brophy, C. M., Werner, L. S., and Sinibaldi, J. O., "Performance Characterization of a Valveless Pulse Detonation Engine," AIAA Paper 2003-1344, Jan. 2003.

[13] Mattison, D. W., Liu, J. T. C., Jeffries, J. B., Hanson, R. K., Brophy, C. M., and Sinibaldi, J. O., "Tunable Diode-Laser Temperature Sensor for Evaluation of a Valveless Pulse Detonation Engine," AIAA Paper 2005-0224, Jan. 2005.

[14] Brophy, C. M., and Hanson, R. K., "Fuel Distribution Effects on Pulse Detonation Engine Operation and Performance," *Journal of Propulsion and Power*, Vol. 22, No. 6, 2006, pp. 1155–1161. doi:10.2514/1.18713

[15] Piton, D., Prigent, A., Serre, L., and Monjaret, C., "Performance of a Valveless Airbreathing Pulse Detonation Engine," AIAA Paper 2004-3749, July 2004.

[16] Ma, F. H., and Yang, V., "A Unified Flow Analysis of Valveless Airbreathing Pulse Detonation Engine," *Pulse and Continuous Detonation Propulsion*, edited by G. Roy, and S. Frolov, Torus Press, Moscow, Russia, 2006, pp. 219–234.

[17] Ma, F. H., Choi, J. Y., and Yang, V., "Internal Flow Dynamics and Performance of Valveless Airbreathing Pulse Detonation Engine," AIAA Paper 2006-1024, Jan. 2006.

[18] McBride, B. J., and Gordon, S., "Computer Program for Calculation of Complex Chemical Equilibrium Compositions and Applications," NASA, Reference Publication 1311, June 1996.

[19] Wang, X. Y., and Chang, S. C., "A 2D Non-Splitting Unstructured Triangular Mesh Euler Solver Based on the Space-Time Conservation Element and Solution Element Method," *Computational Fluid Dynamic Journal*, Vol. 8, No. 2, 1999, pp. 309–325.

[20] Wu, Y. H., Ma, F. H., and Yang, V., "Space-Time Method for Detonation Problems with Finite-Rate Chemical Kinetics," *International Journal of Computational Fluid Dynamics*, Vol. 18, No. 3, 2004, pp. 277–287. doi:10.1080/10618560310001623340

[21] Karypis, G., and Kumar, V., "Multilevel K-Way Partitioning Scheme for Irregular Graphs," *Journal of Parallel and Distributed Computing*, Vol. 48, No. 1, 1998, pp. 96–129. doi:10.1006/jpdc.1997.1404

[22] Choi, J. Y., Ma, F. H., and Yang, V., "Some Numerical Issues on Simulation of Detonation-Cell Structures," *Combustion, Explosion, and Shock Waves* (to be published).

[23] Roache, P. J., "Quantification of Uncertainty in Computational Fluid Dynamics," *Annual Review of Fluid Mechanics*, Vol. 29, 1997, pp. 123–160.

[24] Roache, P. J., "Verification of Code and Calculations," *AIAA Journal*, Vol. 36, No. 5, 1998, pp. 696–702.

[25] Culick, F. E. C., and Rogers, T., "The Response of Normal Shocks in Diffusers," *AIAA Journal*, Vol. 21, No. 10, 1983, pp. 1382–1390.

[26] Oh, J. Y., Ma, F. H., Hsieh, S. Y., and Yang, V., "Interactions Between Shock and Acoustic Waves in a Supersonic Inlet Diffuser," *Journal of Propulsion and Power*, Vol. 21, No. 3, 2005, pp. 486–495.

J. Powers
Associate Editor